Contents lists available at ScienceDirect

Applied Surface Science

Full Length Article

Impact of sub-grain structure on radiation resistance in additively manufactured 316L stainless steels: An atomic insight into the mechanism

Changyuan Li [a], Feida Chen [a,b,*], Guojia Ge [a], Jiwei Lin [a], Zhangjie Sun [a], Minyu Fan [c], Ping Huang [c], Xiaobin Tang [a,b,*]

[a] *Department of Nuclear Science & Technology, Nanjing University of Aeronautics and Astronautics, Nanjing 211106, China*
[b] *Key Laboratory of Nuclear Technology Application and Radiation Protection in Astronautics, Ministry of Industry and Information Technology, Nanjing 211106, China*
[c] *Suzhou Nuclear Power Research Institute, Suzhou 215004, China*

ARTICLE INFO

ABSTRACT

Laser-based additive manufacturing (AM) provides a new pathway for rapid manufacturing of radiation-resistant materials used in the nuclear engineering system. Ultrafine sub-grain boundary (SGB) structure in AM materials plays an important role in enhancing radiation resistance of materials. Here, we combined experimental and molecular dynamics simulation methods to investigate the interaction between cellular SGBs in AM 316L stainless steel (SS) and irradiation-induced defects. Experimental results prove that the laser powder-bed-fusion (L-PBF) 316L SS presents a more uniform distribution of the defect sizes and the mean defect size is smaller after irradiation compared with cold-rolled (CR) 316L SS. The energetics and dynamics simulation results show that the SGB structure is an efficient sinking site for interstitial atoms. Density of dislocation network on SGBs exerted a significant effect on the reduction of interstitial atom formation energy near SGBs. After irradiation, the evident increase of SGB volume ratio fails to improve the defect self-healing performance but reduces the dislocation density on the SGB, thereby impairing the radiation resistance of the material. This work provides an insight into better understanding of the AM radiation enhanced materials from the combination of atomic simulation and irradiation experiments.

1. Introduction

Research on nuclear engineering materials today is facing unprecedented pressure – not only to improve the performance of structural materials to adapt to increasingly extreme service conditions [1-3], but also to control costs to meet the economics of nuclear power and improve its competitiveness with other energy sources. Nuclear material researchers have been investigating the interface for decades to create structural materials with high radiation tolerance since the discovery of the self-healing effect of interfaces on radiation defects of the material. For example, typical radiation-resistant materials, such as nano-oxide dispersion strengthened steels (ODSs) [4-6], nanoscale metallic multilayers [7-9], and graphene-reinforced metal matrix nanocomposites (GRMMNCs) [10-12], have been developed in recent years and achieved excellent radiation defects suppressing performance by introducing ultrahigh-density interfaces. However, the majority of interface structures can only be prepared under precise laboratory conditions and under careful manipulation of researchers. The case of nanoscale

metallic multilayers is a typical example that grows at a rate of approximately 10 nm/min in a clean room. Such slow processing speeds and high costs indicate the poor applicability of these materials in the field of nuclear engineering.

Laser-based additive manufacturing (AM), a revolutionary key strategic technology, has attracted considerable research attention in recent years [13]. Laser-based AM substantially reduces processing procedures and the number of parts of equipment of complex three-dimensional structures, thereby reducing the risk of failure and the difficulty of inspection due to the presence of an excessive number of weak links in the equipment. Nuclear material researchers and manufacturers have also explored laser-based AM due to its satisfactory properties [14-16]. However, unlike other traditional manufacturing processes, laser-based AM can be regarded not only as an advanced manufacturing technology for industrial sustainability but also a potential innovative technology that can provide a new pathway for the rapid manufacturing of radiation-resistant nanointerface structural materials.

At present, many studies have discovered an interesting structure

---

called nano-cellular sub-grain boundaries (SGBs) spontaneously and rapidly form in additive manufacturing materials [17-19], which likely exert a beneficial effect on inhibiting the growth of radiation defects [20-22]. Regarding this unique structure, researchers have carried out a lot of work into its radiation resistance. The high fluence irradiation experiment on AM 316LN stainless steel (SS) by Zhang et al. reveals the good radiation resistance of AM materials [23]. They also found the SGBs can serve as effective defect sinks to reduce the dislocation loop density through in-situ irradiation observation, and the dislocations climbing on SGBs causes its diffusion during the irradiation [24]. In our previous work, the He bubble density and irradiation hardening degree of AM 316 L SS have proved to be lower than that of cold-rolled 316 L SS [25,26]. Wang et al. confirmed that the dislocations on SGBs can serve as trapping sites for irradiation-induced defects by in-situ observation of dislocation reactions [27]. With the development of laser-based AM technology entering new stages, researchers have begun to discuss the possibility of precise control of the density and structural characteristics of nano-cellular SGBs in AM materials [28]. A deep understanding of the atomic mechanism of the interaction between nano-cellular SGBs and radiation defects is crucial at this stage.

In this work, the 316L SS was selected as the prototype material. On the one hand, 316L SS has been extensively used in the fuel assembly components and primary coolant pipes under harsh radiation environments. On the other hand, 316L SS is also a mature material for laser-based AM. We combined experimental investigations and molecular dynamics simulations to discuss the interaction mechanism between cellular SGBs in AM 316L SS and radiation defects caused by cascade collisions. We showed that riverbed-like low-angle SGBs, high-density dislocation network structure, and element segregation constitute the unique cellular SGB configuration of AM 316L SS. The evolution of irradiation-induced dislocation loops was significantly affected by SGBs. The interaction behavior and mechanism between radiation defects and SGBs were investigated in detail through energetics and dynamics simulation. Our results show that the evolution of point defects and dislocation loops in AM 316L SS is regulated by the dislocation density and configuration of SGBs.

2. Materials and methods

2.1. Material fabrication

The L-PBF 316L SS samples were fabricated on the BLT-A300 machine with a maximum power of 500 W. All the additive manufacturing samples were printed on the steel substrate under argon atmosphere, with the size of 30 mm × 30 mm × 50 mm. The scanning strategy adopted cross hatching. A longer laser vector was set to reduce the coincidence in adjacent layers, and the laser scanning direction was rotated clockwise by 67° level-by-level. Detailed process parameters applied in the construction of porosity-free material are listed in Table 1. Commercial 316L powders suitable for L-PBF (particle size of 30–50 μm) were used as raw materials in this study. The chemical composition of 316L powder is presented in Table 2. Traditional commercial cold-rolled 316L SS was purchased from Wuxi Xinguangda Steel Co., Ltd. The cold-rolled samples were solution annealed at 1373 K for 2 h to eliminate the original defects and carbides, and the vacuum degree was less than 10^{-5} Pa. After annealing, the samples were cold-rolled with 15% deformation.

Table 1
The process parameters we applied in the building process.

Power (W)	Scanning rate (mm/s)	Line spacing (mm)	Spot diameter (μm)
190	1000	0.06	70

2.2. Irradiation experiments and characterization

Materials are mainly irradiated by neutrons in the reactor, which collide with lattice atoms causing radiation damage. However, neutron irradiation requires a long experimental period to produce enough damage, and it may cause induced radioactivity, which needs a long time to place for experimental observation. Ion irradiation can generate enough damage in a short time without inducing radioactivity [29]. It's the best alternative to neutron irradiation. The damage depth of ion irradiation can be simulated by SIRM. Fig. 1 shows the Ar^{8+} ion damage profile and implanted atom concentration calculated by SRIM-2008 [30] at the Quick Kinchin-Pease mode. It shows the damage range of Ar^{8+} ion is 18 nm, which means the equivalent damage of 3.7dpa under neutron irradiation can be achieved at 18 nm in the ion implantation.

The EBSD test adopted FEI Quanta 450 feg field emission scanning electron microscope, with the tube voltage of 20 kV, scanning step of 0.5 μm and step width of 17.6 mm. Specimens for the irradiation experiment were prepared using a standard double-jet procedure (7 vol. % per-chloric acid and 93 vol% ethanol with a voltage of 65 V at − 25 °C) to facilitate the following TEM observation. Ar ions irradiation experiment was performed in a 100 kV ion implanter at the Special Equipment Safety Supervision Inspection Institute of Jiangsu Province. Specimens were irradiated with 80 keV Ar ions to achieve 3.7 dpa at RT. Conventional TEM imaging was performed on all specimens using a Tecnai G2 F20 S-Twin with a maximum accelerating voltage of 200 kV.

2.3. Molecular dynamics simulation

Molecular dynamics simulations were performed using a large-scale atom/molecule massively parallel simulator (LAMMPS) [31]. Embedded atom method (EAM) potential developed Bonny [32] in 2013 was used in our study for Fe, Cr, and Ni ternary alloys. This potential is an improved version of the simulation of radiation defect evolution. Energetic validation of the EAM potential in our work is presented in Table S1. The FeCrNi alloy Fe–11Ni–18Cr with a face-centered cubic (FCC) crystal was used to simplify the simulation and represent 316L SS. A lattice constant of 3.5736 Å was calculated using a model of 20 by 20 by 20 lattice units and relaxed at 300 K for 400 ps.

In this paper, the open-source atomic modeling software ATOMSK (Hirel, 2015) [33] was used for simulation modeling. Fig. 2 shows the configuration of the L-PBF 316L SS model. The size of model was set to $90 \times 115 \times 30$ units, which contained 622,893 atoms. The crystallographic direction along the x-axis was set to $[10\bar{1}]$, the y-axis was [010] and the z-axis was [101]. So that the dislocations on the SGBs were not limited by the periodic boundary conditions imposed on the simulation box and moved freely on the $(11\bar{1})$ and $(\bar{1}11)$ slip planes. Four sub-grains with different directions were added in the simulation box (Fig. 2(a)), and the rotation angles of sub-grains are shown in Table 3. Based on the chemical compositions listed in Table 4, the SGBs with high-density dislocations were added between the sub-grains. The width of SGBs were maintained at 30 Å and high-density dislocations were inserted every 5 Å along the y-axis inside SGBs. Dislocation lines after relaxation showed a parallel arrangement very similar to the configuration observed in Kong et al. [34]. Meanwhile, a conventional LAGB model without dislocation network inside the sub-grain boundaries was built as the control model. The detailed information of control models was provided in the supplementary material.

The formation energy of point defect was calculated by adding or deleting an atom near the simulation system. The interstitial atoms were added to the octahedral void of FCC lattice. The formation energy of defect is expressed as follows:
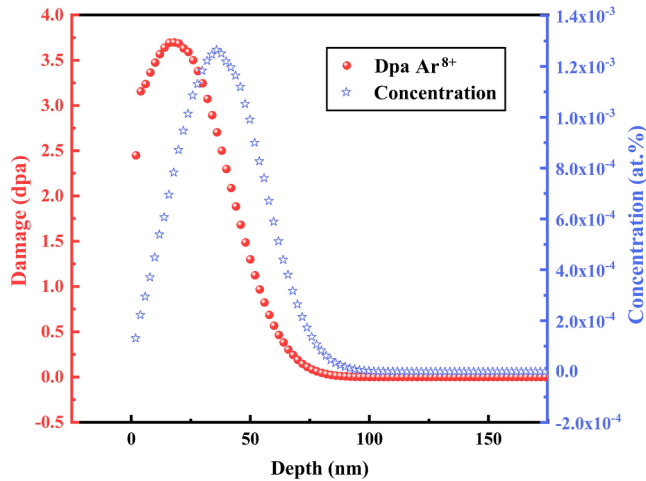
$$E_f^\alpha = E_{GB}^\alpha - E_{GB} \pm E_{coh}, \qquad (1)$$

where E_{GB}^α and E_{GB} are the total energy of the system before and after adding defects, respectively, and E_{coh} is the cohesive energy of a perfect

Table 2
The chemical composition of 316L powder (wt.%).

	Cr	Ni	Mo	Mn	Si	C	S	P	Fe
L-PBF	17.17	10.45	2.22	1.20	0.52	0.017	0.014	0.031	Bal.
CR	16.64	10.05	2.02	1.18	0.44	0.020	0.002	0.031	Bal.

Fig. 1. SRIM calculated Ar^{8+} damage profile (red line) and ion implantation profile (blue line).

system without defects. The sign in Eq. (1) is positive when calculating the vacancy and negative when calculating the interstitial atom [35,36].

Cascade collision simulation was performed under microcanonical thermodynamic ensemble (NVE). A Berendsen thermostat of 300 K was applied to the frozen region surrounding the system to dissipate the energy introduced by the primary knock-on atom (PKA). An Fe atom inside the sub-grain was selected randomly as the PKA, and an energy of 1–15 keV was provided to move toward SGBs. The entire simulation time was approximately 50 ps, and a variable time step setting was used to prevent the loss of atoms caused by a large step in the initial stage of the cascade collision. To reduce errors, five effective simulations were conducted at each energy value to ensure the validity of data.
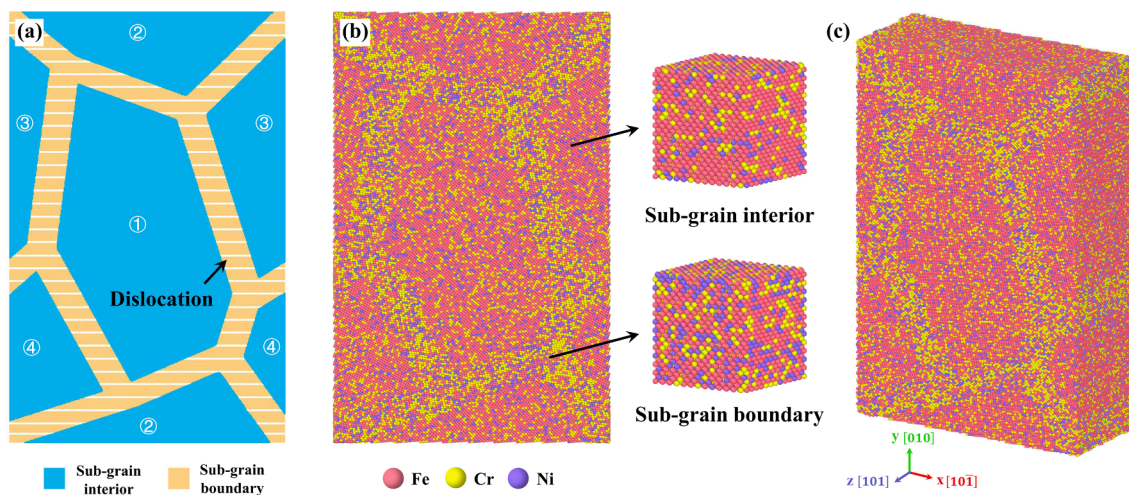
3. Results and discussion

3.1. Microstructure changes of L-PBF 316L SS exposed to ion irradiation

Fig. 3(a) shows the as-prepared L-PBF 316L SS samples, on the basis of which a series of experiments and tests were carried out. Fig. 3(e) shows the EBSD analysis results, which indicated the existence of SGBs. Grain orientation spread (GOS) figure [37] showed that the average deviation in the orientation between each point in a grain and the average orientation of the grain in the case of L-PBF 316L SS is larger than that in the case of CR 316L SS. However, kernel average misorientation (KAM) figure showed that misorientations of points in a grain in the L-PBF 316L SS are generally as low as those in the case of CR 316L SS when a similar analysis is performed within a kernel. The difference of KAM figure between L-PBF and CR cases is that many kernels in L-PBF 316L SS present higher misorientations that likely contain SGBs. Fig. 4 (a) clearly shows the TEM image of nano-cellular sub-grain structure on the scan plan of the as-prepared L-PBF 316L SS. L-PBF 316L SS presents ultrahigh density of riverbed-like SGBs with high-density dislocation network, which indicates that the configuration of SGBs with chaotic dislocation structure is completely different from sharp GBs observed in traditional metallic materials. Fig. 3(b)-(d) show that these SGBs are

Table 3
Rotation angle of sub-grains along the z-axis.

Sub-grain number	①	②	③	④
Rotation angle	10°	5°	15°	20°

Table 4
Atomic percentages of Cr and Ni in sub-grain interior and sub-grain boundaries (at%).

	Sub-grain interior	Sub-grain boundaries
Cr	18	26
Ni	11	17

Fig. 2. Atomic model of L-PBF 316L SS: (a) configuration of the sub-grain interior and SGB, (b) atomic configuration of the computational cell, (c) 3-D view of the computational cell.
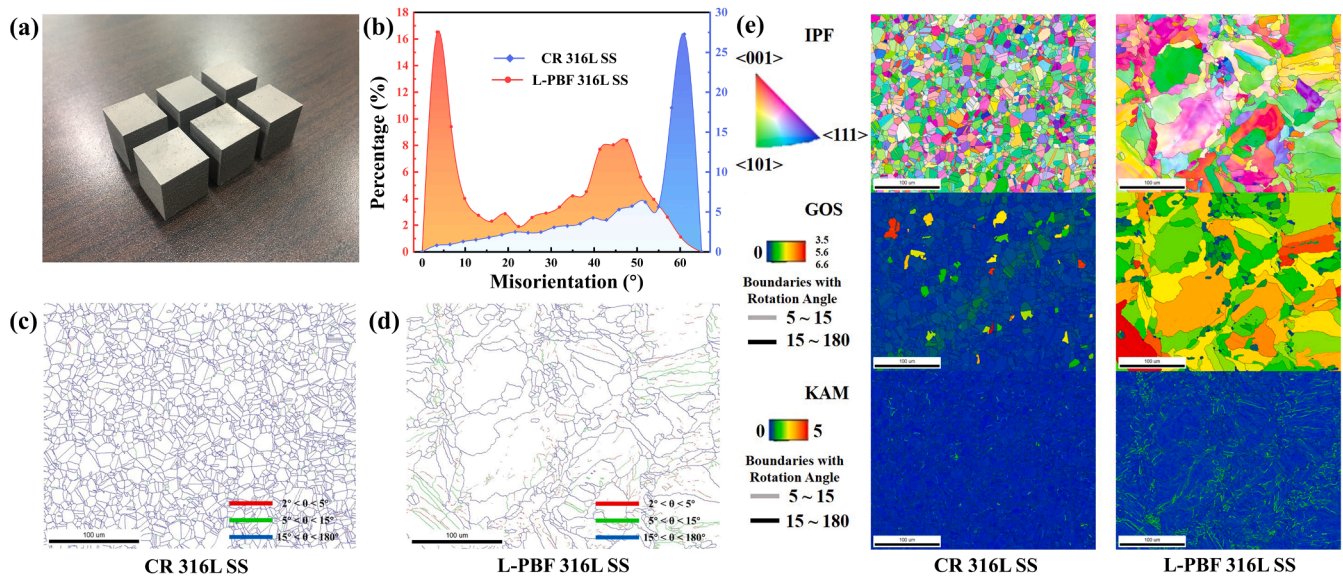
Fig. 3. Microstructure properties of L-PBF 316L SS and CR 316L SS: (a) picture of as-prepared L-PBF 316L SS, (b) misorientation of GBs in L-PBF 316L SS and CR 316L SS, (c) misorientation characteristic of GBs in CR 316L SS, (d) misorientation characteristic of GBs in L-PBF 316L SS, (e) EBSD results of CR 316L SS and L-PBF 316L SS.
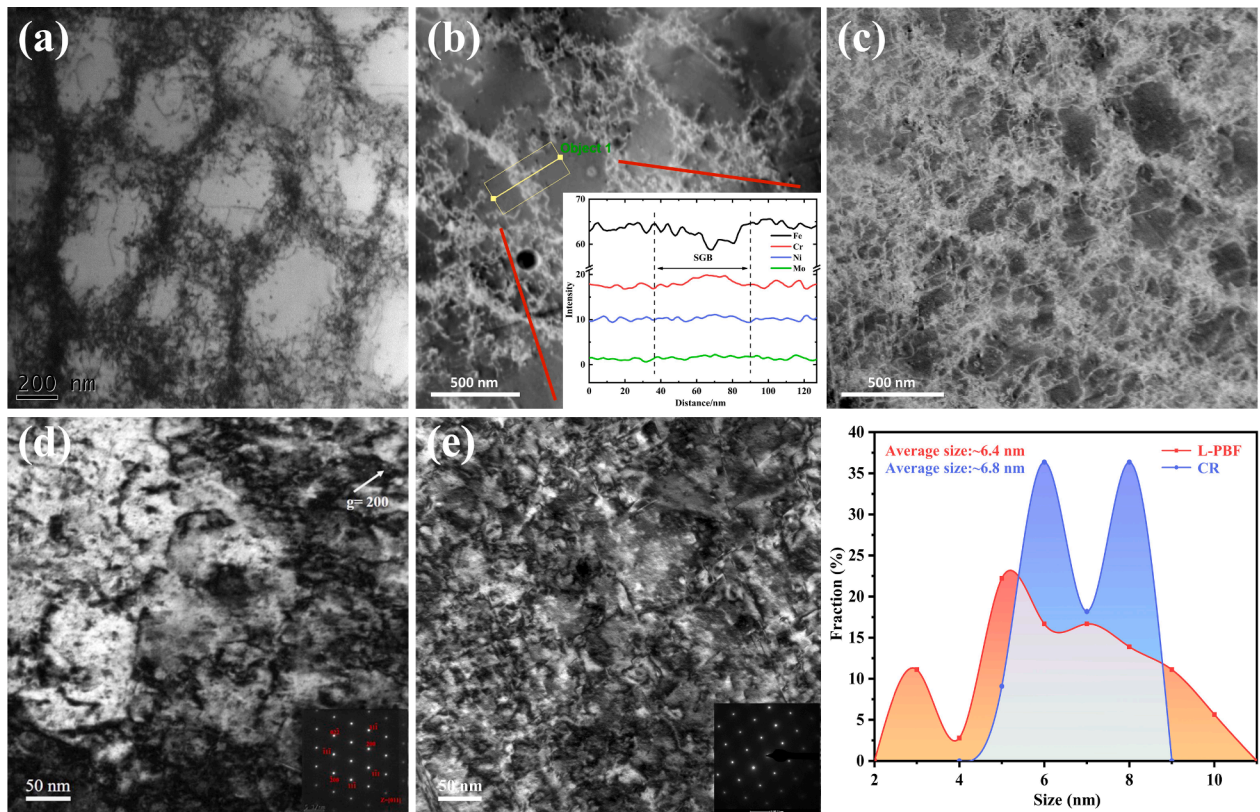

Fig. 4. Microstructure of as-prepared and irradiated L-PBF 316L SSs: (a) cellular SBGs of the as-prepared L-PBF 316L SS, (b) element distribution across SBGs of the as-prepared L-PBF 316L SS, (c) diffused cellular SGBs in Ar ion-irradiated L-PBF 316L SS, (d) TEM image of dislocation loops induced by irradiation in L-PBF 316L SS, (e) TEM image of dislocation loops induced by irradiation in CR 316L SS.

essentially LAGBs with a misorientation of 2°–15°. The detailed configuration of the dislocation network is hard to characterize because the dislocation density is excessively high. Line scan analysis was instead performed on SGBs to explore the element segregation at SGBs (Fig. 4 (b)). The rapid solidification of L-PBF process leads the ferrite stabilizers like Mo, Cr and Si to be ejected from the liquid along the solid–liquid

interface and trapped at the SGBs [38,39]. The results showed that Cr, Ni, Mn, and Mo were enriched at SGBs while Fe was depleted. During directional solidification, the constitutional stress caused by solute enrichment led to the deformation, which was accommodated by dislocations [28], thereby promoting the formation of dislocation network on SGBs.

Fig. 4(c) presents the microstructure of the L-PBF 316L SS foil specimen after exposure to Ar ion irradiation to 3.7 dpa at RT. The result was similar to what Zhang got in their work [24], in which the nano-cellular sub-grain structure remains intact, but dislocation network wrapped around SGBs significantly diffuse into the interior of the sub-grain. On the other hand, as shown in Fig. 4(d) and (e), dislocation loops in irradiated L-PBF 316L and CR 316L SSs were observed under the condition of [0 1 1] zone axis with g = 200. After careful observation of at least 10 different zones in each specimen, we observed that the number density and the average size of radiation induce dislocation loops of 4.7×10^{21} m^{-3} and 6.4 nm in L-PBF 316L SS and 1.5×10^{21} m^{-3} and 6.8 nm in the case of CR 316L SS, respectively. Notably, dislocation lines in both cases were not counted because of the difficulty in determining whether such lines were generated by irradiation. Compared with CR 316L SS, L-PBF 316L SS presents a more uniform distribution of the defect sizes and the mean defect size is smaller after irradiation. According to the previous in-situ experimental study [27], this is mainly attributed to the effect of SGBs that makes L-PBF 316L SS exhibits a better radiation resistance. However, a deep understanding on the evolution mechanism of these radiation defects and the interaction between radiation defects and SGBs need to be further explored.

3.2. Evolution behaviors of radiation defects and dislocation network

Since we showed above that the riverbed-like low-angle SGBs, high-density dislocation network structure and element segregation constitute the unique cellular SGB configuration of L-PBF 316L SS, an atomic model of L-PBF 316L SS with high-density dislocation network was built and leveraged to explore evolution behaviors and mechanism of the dislocation network and radiation defects further though molecular dynamics simulation. Notably, simulation models were smaller than the real size due to the limitation of the computational ability. Here, basic modeling principles were set to ensure the accuracy of simulation results, the ratio of the SGB width to the sub-grain width and the ratio of the SGB width to the interval of dislocation inside SGBs remained constant with the configuration observed in experiments.

Wigner–Seitz defect analysis [40] in the visualization software OVITO [41] was applied to observe the cascade collision process. Fig. 5 (a) and (b) show that residual vacancies are more than interstitial atoms at the end stage of the cascade collision in both models. The difference of residual defects between L-PBF 316L SS and LAGB control group is shown in Fig. 5(c). A clear trend revealed that SGB exerts an inhibitory effect on the radiation damage, which reconfirmed the experiment results that the radiation resistance of L-PBF 316L SS is better than that of CR 316L SS. Fig. 6(a) presents the microstructure evolution of high-density dislocation network at different stages of the cascade collision with 15 keV PKA. Although the PKA bombardment causes serious damage to dislocation network around SBGs at the beginning of the cascade collision, the dislocation network gradually returned to its original state with the process of cascade collision annealing stage and a clear interface can be recognized at 40 ps. The comparison of the configuration of 1 ns after cascade collision showed that final dislocation network maintained a stable state. The excellent strength performance of AM 316L SS mainly originated from the cellular sub-grain structure [42], and the recovery of the cellular dislocation network structure after cascade collision assured the long-term service reliability of material under radiation environment. Furthermore, the observation of irradiation-induced dislocation loops revealed that it formed a defect depletion region near SGBs at the final stage of evolution, which showed the strong interaction between SGBs and irradiation-induced dislocation loops throughout the evolution process.

Fig. 6(b) shows the development of the dislocation length at each moment of the cascade collision. Within 1 ps, the PKA with high energy made a large number of atoms deviate from the lattice equilibrium position, and the dislocation structure on the sub-grain boundary was destroyed, and all dislocations lengths are obviously reduced at 1 ps.
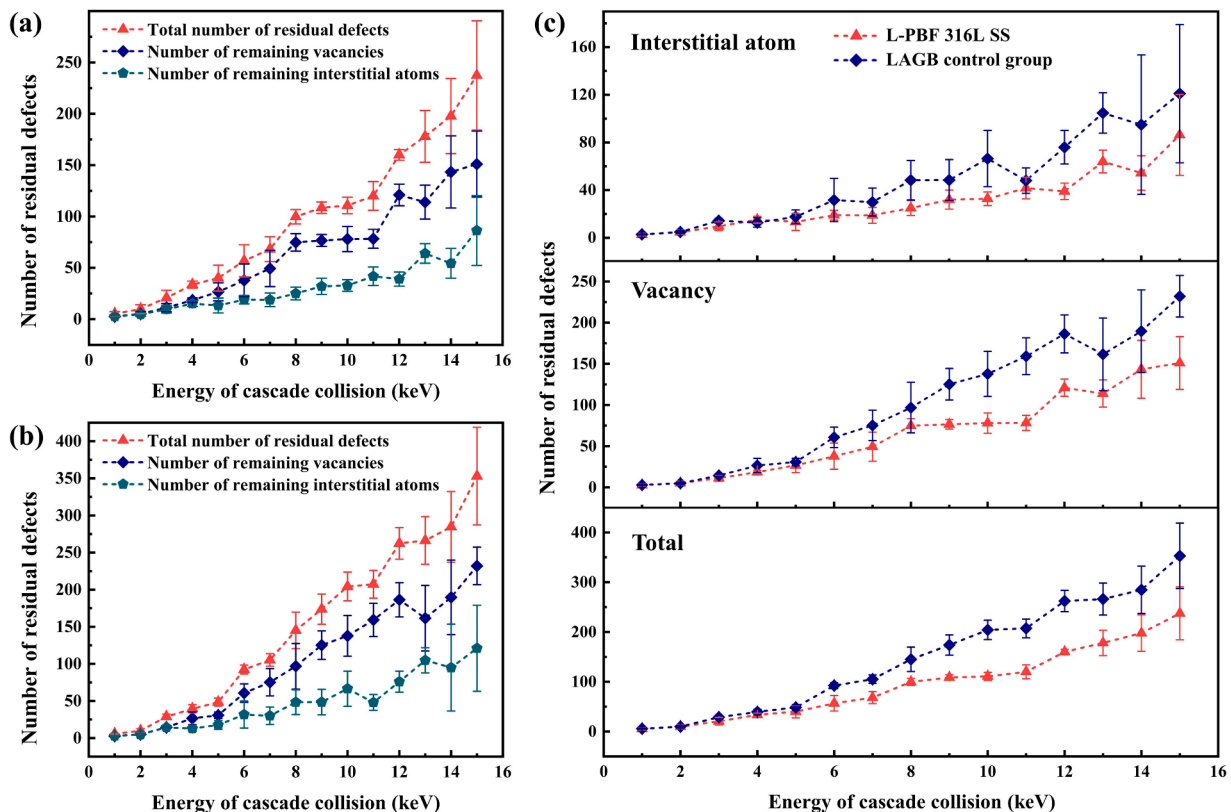

Fig. 5. Number of residual defects after cascade collision: (a) L-PBF 316L SS, (b) LAGB control group, (c) comparison of residual defects. Dashed lines in the figure visualize the trend of the curve. The detailed cascade collision process with 3 keV PKA is available in supplementary video.
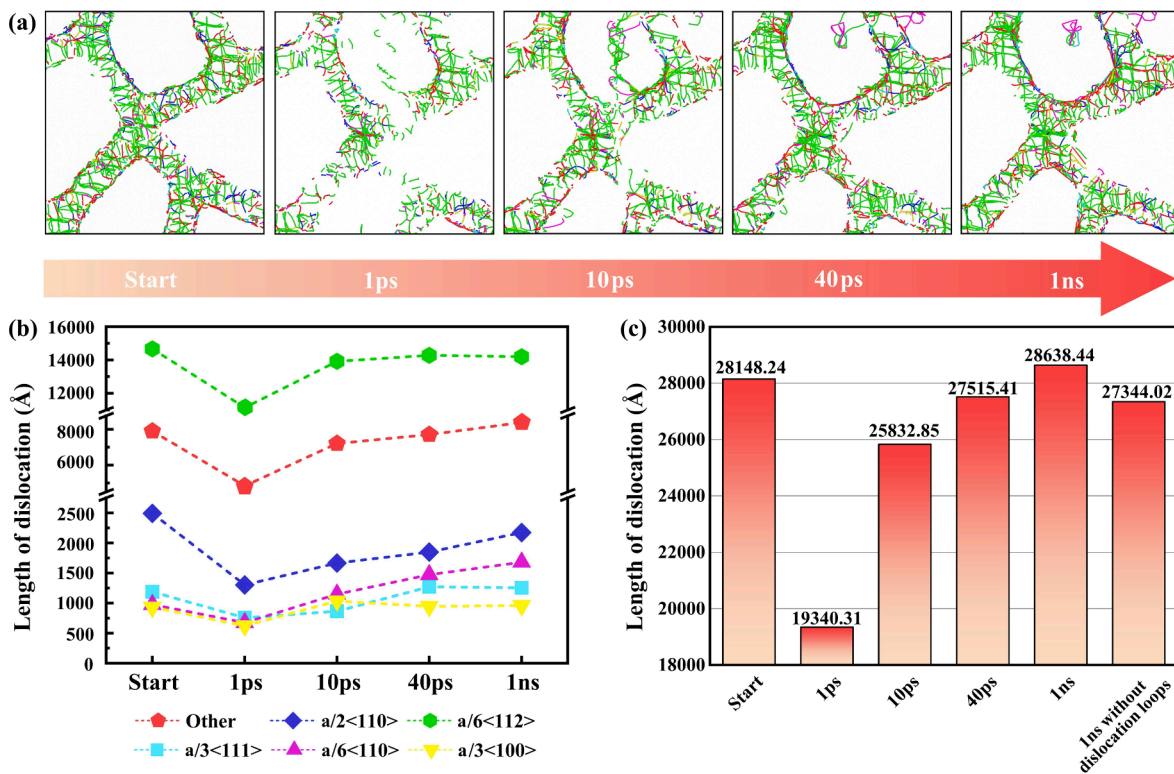
Fig. 6. Microstructure development of L-PBF 316L SS during cascade collision: (a) microstructure evolution of high-density dislocation network, (b) development of dislocation lengths of all types, and (c) development of total dislocation length. All atoms are removed from the Fig. 6(a), and only the dislocation line calculated via Dislocation Extraction Algorithm [43] analysis remained. The same colors were used to identify dislocations in Fig. 6(a) and 6(b).

After 10 ps, the length of dislocation gradually increased due to the evolution of defects caused by cascade collision. During the annealing stage within 40 ps, A large number of dislocations were recovered through the following dislocation reactions but still failed to reach the original level. The face-centered cubic metal mainly contains a/6 ⟨1 1 2⟩ Shockley partial dislocation and a/3 ⟨1 1 1⟩ Frank partial dislocation [42,44]. During cascade collision annealing, the dislocation length of Shockley partial dislocation which can't climb recovered to the original level, and the length of movable Frank partial dislocation increased. From 40 ps to 1 ns, the a/6 ⟨1 1 2⟩ Shockley and a/3 ⟨1 1 1⟩ Frank dislocations transformed into a/2 ⟨1 1 0⟩ perfect dislocations, and the length of a/6 ⟨1 1 0⟩ acute-angle stair-rod dislocation also increased due to the slip and recombination of dislocations. The morphology and dislocation types of dislocation network continue to develop towards intact and low energy stable states.

Fig. 6(c) presents the total length of the dislocation network. The total length of dislocations reached 28,638.447 Å, which was approximately 101.74% of the original length, at 1 ns after the cascade collision. However, this value includes the length of dislocation loops generated by the cascade collision inside SGBs. The total length remained at 27,344.025 Å, which was approximately 97.14% of original level, after removing the dislocation loop length. After a long-time cascade collision annealing stage, the total length and morphology of dislocation network in SGBs nearly recovers to the original state, which means the dislocation density on SGBs almost maintains the same after cascade collision. These results indicated that the radiation damage of high-density dislocation network is weak. The microstructure of L-PBF 316L SS exhibits excellent radiation tolerance. At present, the phenomena of SGBs diffusion are still difficult to obtain in the limited cascade collision simulations with molecular dynamics. Further simulation needs to be combined with mesoscopic methods such as kinetic monte carlo.

3.3. Energetic mechanism of cellular SGBs in L-PBF 316L SS

The SGB models used for energetic simulation include linear and cross-type. Fig. 7(a) presents the formation energy near the cross-type SGBs. The energy drop region of the interstitial atom was larger in the SGB model than that of the LAGB control group and distributed continuously near SGBs, thereby indicating its satisfactory ability to capture interstitial atoms. Both SGB and control models showed weak ability to capture vacancies after excluding intrinsic defects, which exhibited significant characteristics of biased sinks. The distribution of defect formation energy near linear SGBs is shown in Fig. 7(b)–(d). Compared with that in the control group, the energy drop region in the SGB model was larger and the formation energy of defects inside sub-grain was lower. However, amplitudes of energy drop of interstitial atoms was similar in both models. This finding proved that the dislocation type at sub-grain boundaries exerts minor effect on the formation energy and the main effect comes from the density of dislocations on boundaries, which determines the energy drop region of interstitial atoms and the formation energy of defects inside sub-grain.

Fig. 7(e) illustrates the average atomic potential energy and the distribution of atomic potential energy. The result showed that the L-PBF 316L SS presents not only a high average potential energy but also a significant increase in potential energy near SGBs. The average potential energy is related to the possibility of atoms passing through the energy potential well [45]. A high atomic potential energy allows additional atoms to migrate to nearby locations via thermal motion and facilitates the diffusion process in L-PBF 316L SS [46]. In addition, a large number of radiation-induced interstitial atoms were trapped by SGBs due to their strong capability of trapping interstitial atoms. The aggregation of interstitial atoms on SGBs increased the probability of recombination with nearby vacancies and promoted the self-healing process of radiation-induced defects [47]. The high dislocation density caused by SGBs accelerates the migration and self-healing of defects, making L-PBF
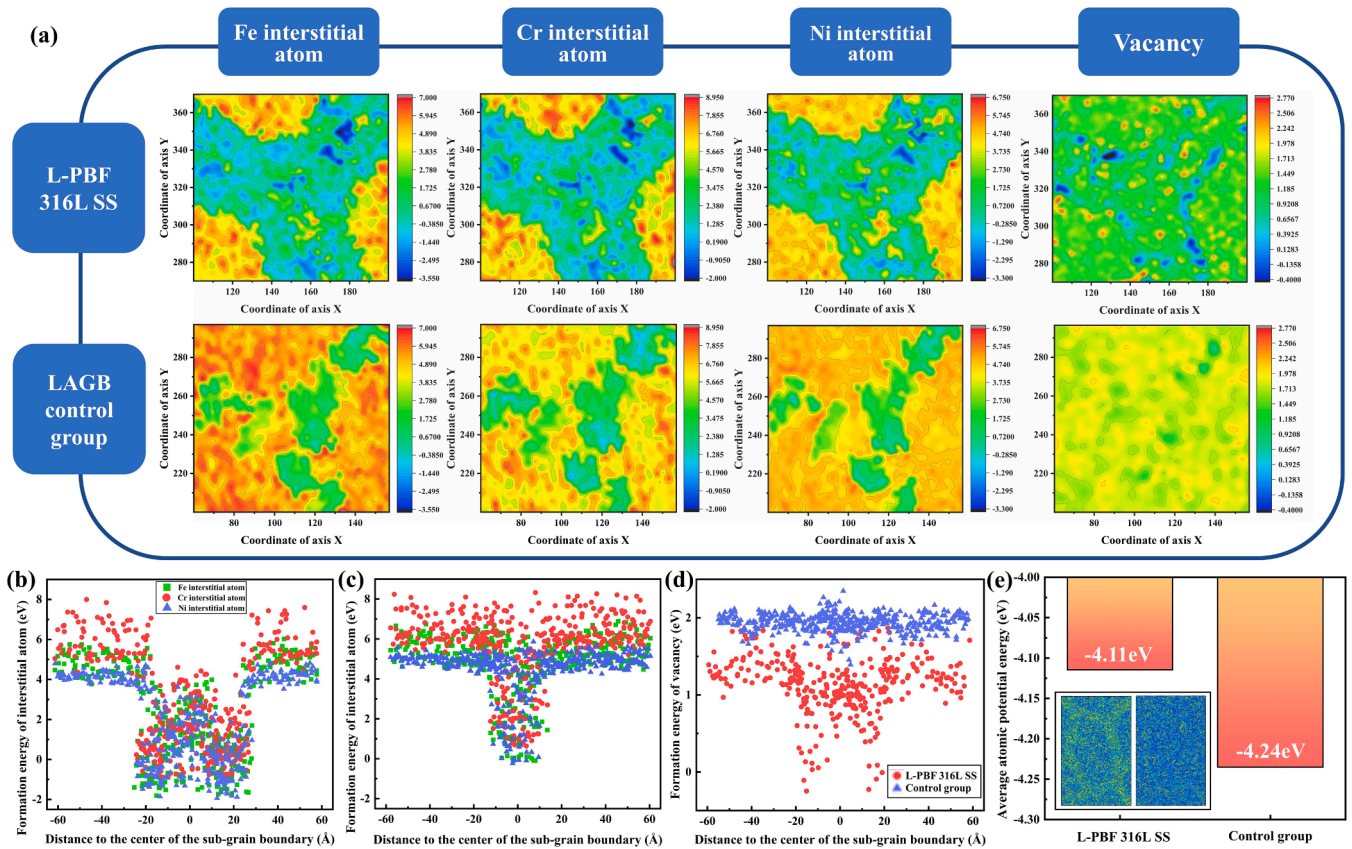
Fig. 7. Energetic analyses of cellular SGBs: (a) formation energy of defects near the cross-type SGBs, (b) formation energy of interstitial atoms near the linear SGB in L-PBF 316L SS, (c) formation energy of interstitial atoms near the linear LAGB in the control group, (d) formation energy of vacancy, and (e) average energy of atomic potential. The distribution of atomic potential is shown in Fig. 7(e), with L-PBF 316L SS on the left and the control group on the right. Bright colors of atoms indicate high energy.
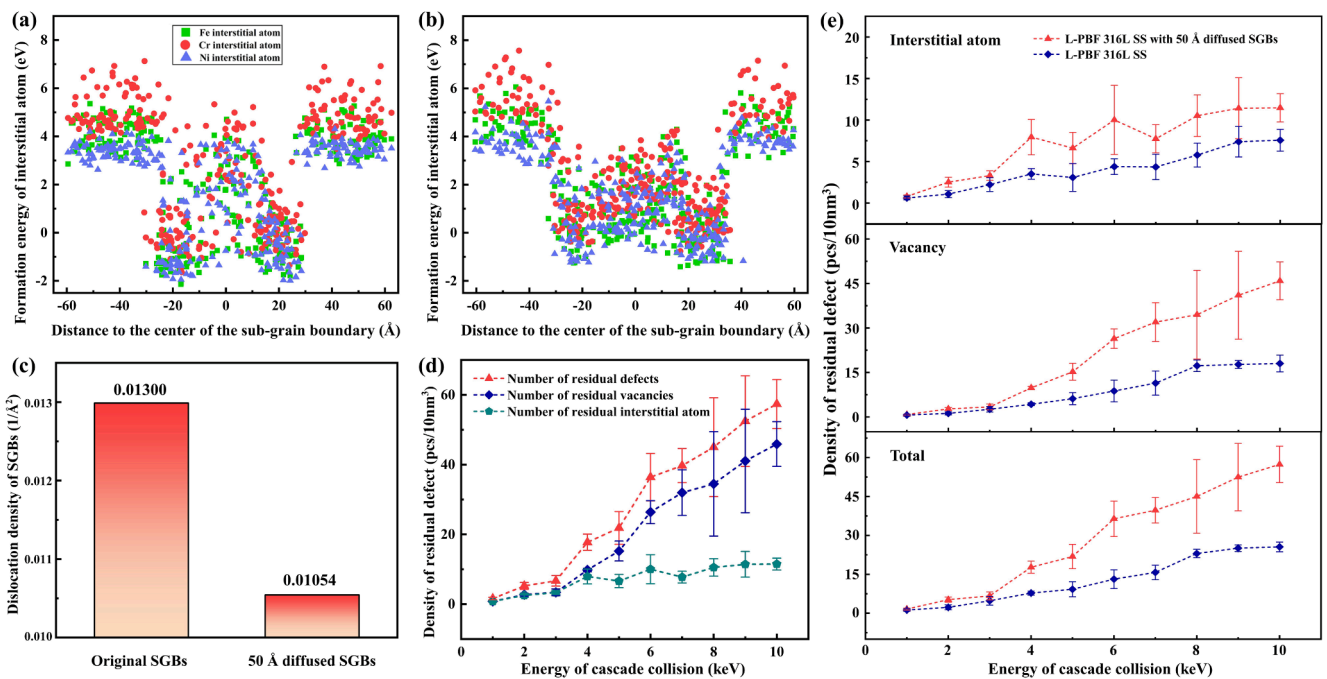

Fig. 8. Energetics analyses and density of residual defects of diffused L-PBF 316L SS: (a) formation energy of interstitial atoms near the 40 Å diffused SGBs, (b) formation energy of interstitial atoms near the 50 Å diffused SGBs, (c) dislocation density near SGBs, (d) density of residual defects near the 50 Å diffused SGBs, (e) comparison of the residual defects density.

316L SS have excellent radiation resistance.

3.4. Influence of diffused cellular SGBs on the defect sinking effect

Actively or passively regulating the configuration of SGBs will exert a significant influence on interaction behaviors with radiation defects given that the defect trapping capacity and energy state of SGBs present highly sensitive responses to the dislocation density of SGBs. Researchers have characterized the high density of dislocations network inside the SGBs have a high tendency to dissociate, which tends to form wider stacking faults [48]. Fig. 4(c) shows that the dislocation wrapped around SGBs significantly diffuses into the interior of the sub-grain, which causes the change of dislocation morphology of SGBs, although the integrity of SGBs remains undamaged during the irradiation process. Here, two L-PBF 316L SS models with 40 Å and 50 Å diffused SGBs (detailed information is provided in supplementary material) were used to discuss the influence of diffused cellular SGBs on the sinking defect.

Fig. 8(a) and (b) show the formation energy of interstitial atoms near diffused linear SGBs. Although the energy dropping region of interstitial atoms increased from 40 Å to 50 and 60 Å, weaker amplitudes of energy drop of diffused SGBs than the original, which indicates the decline of interstitial atoms trapping ability. The dislocation density near the SGBs is shown in Fig. 8(c). The results indicated that the decrease of dislocation density in the diffused SGBs was the main reason for the effect on the formation energy of interstitial atoms. Fig. 8(d) and (e) present the results of cascade collision simulation in the 50 Å diffused SGBs model. The density of residual defect was calculated and compared with the previous results. The density of total residual defects, interstitial atoms, and vacancies was higher than the previous results. Compared with interstitial atoms, the ability to capture vacancies was obviously weakened after diffusion, which showed the high sensitivity of self-healing performance to dislocation density. The L-PBF 316L SS with diffused SGBs clearly showed weaker radiation resistance than the original one.

According to the simulation here, the defect trapping capacity of diffused SGBs was weakened due to the decreasing dislocation density. The apparent increase of SGB volume ratio fails to improve the self-healing defect performance of the L-PBF 316L SS. By contrast, dislocation diffusion on SGBs reduces the dislocation density on the SGB and significantly changes the energy state near SGBs. Hence, interstitial atoms can no longer be sunk by SGBs when they move to the vicinity of SGBs. Considering the dominant role of dislocation density played in the atomic mechanism of improving the self-healing ability of radiation induced defects in materials, regulating the dislocation density of SGBs actively may provide a feasible pathway to further improve the radiation resistance of AM materials.

4. Conclusions

Our work provided insights into the microstructure of the laser-based AM 316L SS and its microscopic behaviors under irradiation condition. The atomic mechanism of the enhanced radiation tolerance of the laser-based AM 316L SS was investigated using molecular dynamics. The results revealed that the riverbed-like low-angle SGB structure with a certain width is spontaneously formed in laser-based AM 316L SS. The high-density dislocation network surrounds SGBs due to the repeated melting and rapid cooling during the laser-based AM process. Compared with CR 316L SS, the laser-based AM 316L SS presents a more uniform distribution of radiation defects and smaller defect sizes under irradiation conditions. The molecular dynamics results showed a clear drop region of interstitial formation energy near SGBs, thereby indicating the ability of SGBs to trap interstitial atoms from an energetic point of view. The comparison between SGBs and conventional LAGBs indicated that the dislocation type of SGBs exerts a minor effect on the formation energy and the dislocation density on the boundary is the dominant factor. Meanwhile, high-density dislocation network not only can promote the migration of defects m but also inhibit the slip of dislocation loops.

Although the SGB structure enhances the radiation tolerance of laser-based AM 316L SS, dislocation network wrapped around SGBs significantly diffuse into the interior of the sub-grain during the irradiation process. According to our simulation, the decrease of dislocation density on SGBs after dislocation diffusion primarily causes the small formation energy difference between SGBs and the interior of the sub-grain that affects the defect sinking capacity. However, this phenomenon prompts us that actively regulating the configuration of SGBs will also exert a significant influence on its interaction behaviors with radiation defects. The precise control of the dislocation density of SGBs in rapid AM materials can achieve a high level of radiation-tolerant nuclear engineering material with the development of AM technology in the future.

Data availability

No data was used for the research described in the article.

Appendix A. Supplementary material

Supplementary data to this article can be found online at https://doi.org/10.1016/j.apsusc.2022.154926.

References

[1] S.J. Zinkle, G.S. Was, Materials challenges in nuclear energy, Acta Mater. 61 (2013) 735–758, https://doi.org/10.1016/j.actamat.2012.11.004.

[2] I.J. Beyerlein, A. Caro, M.J. Demkowicz, N.A. Mara, A. Misra, B.P. Uberuaga, Radiation damage tolerant nanomaterials, Mater. Today 16 (2013) 443–449, https://doi.org/10.1016/j.mattod.2013.10.019.

[3] S.J. Zinkle, L.L. Snead, Designing radiation resistance in materials for fusion energy, Annu. Rev. Mater. Res. 44 (2014) 1531–7331, https://doi.org/10.1146/annurev-matsci-070813-113627.

[4] X. Zhou, C. Liu, L. Yu, Y. Liu, H. Li, Transformation behavior and microstructural control of high-Cr martensitic/ferritic heat-resistant steels for power and nuclear plants: a review, J. Mater. Sci. Technol. 31 (2015) 235–242, https://doi.org/10.1016/j.jmst.2014.12.001.

[5] M.-L. Lescoat, J. Ribis, Y. Chen, E.A. Marquis, E. Bordas, P. Trocellier, Y. Serruys, A. Gentils, O. Kaïtasov, Y. de Carlan, A. Legris, Radiation-induced Ostwald ripening in oxide dispersion strengthened ferritic steels irradiated at high ion dose, Acta Mater. 78 (2014) 328–340, https://doi.org/10.1016/j.actamat.2014.06.060.

[6] G. Robert Odette, On the status and prospects for nanostructured ferritic alloys for nuclear fission and fusion application with emphasis on the underlying science,

Scr. Mater. 143 (2018) 142–148, https://doi.org/10.1016/j.scriptamat.2017.06.021.

[7] Q.M. Wei, N. Li, N. Mara, M. Nastasi, A. Misra, Suppression of irradiation hardening in nanoscale V/Ag multilayers, Acta Mater. 59 (2011) 6331–6340, https://doi.org/10.1016/j.actamat.2011.06.043.

[8] A.A. Nazeer, M. Madkour, Potential use of smart coatings for corrosion protection of metals and alloys: a review, J. Mol. Liq. 253 (2018) 11–22, https://doi.org/10.1016/j.molliq.2018.01.027.

[9] Y. Chen, N. Li, R.G. Hoagland, X.-Y. Liu, J.K. Baldwin, I.J. Beyerlein, J.Y. Cheng, N. A. Mara, Effects of three-dimensional Cu/Nb interfaces on strengthening and shear banding in nanoscale metallic multilayers, Acta Mater. 199 (2020) 593–601, https://doi.org/10.1016/j.actamat.2020.08.019.

[10] M. Yan, L. Liu, L. Chen, N. Li, Y. Jiang, Z. Xu, M. Jing, Y. Hu, L. Liu, X. Zhang, Radiation resistance of carbon fiber-reinforced epoxy composites optimized synergistically by carbon nanotubes in interface area/matrix, Compos. B Eng. 172 (2019) 447–457, https://doi.org/10.1016/j.compositesb.2019.04.041.

[11] Y. Liu, Y. Zeng, Q. Guo, J. Zhang, Z. Li, D.-B. Xiong, X. Li, D. Zhang, Bulk nanolaminated graphene (reduced graphene oxide)–aluminum composite tolerant of radiation damage, Acta Mater. 196 (2020) 17–29, https://doi.org/10.1016/j.actamat.2020.06.018.

[12] M. Tabandeh-Khorshid, A. Kumar, E. Omrani, C. Kim, P. Rohatgi, Synthesis, characterization, and properties of graphene reinforced metal-matrix nanocomposites, Compos. B Eng. 183 (2020) 107664, https://doi.org/10.1016/j.compositesb.2019.107664.

[13] D. Gu, X. Shi, R. Poprawe, D.L. Bourell, R. Setchi, J. Zhu, Material-structure-performance integrated laser-metal additive manufacturing, Science 372 (2021) 1487, https://doi.org/10.1126/science.abg1487.

[14] N. Sridharan, M.N. Gussev, K.G. Field, Performance of a ferritic/martensitic steel for nuclear reactor applications fabricated using additive manufacturing, J. Nucl. Mater. 521 (2019) 45–55, https://doi.org/10.1016/j.jnucmat.2019.04.020.

[15] L.-E. Rännar, A. Koptyug, J. Olsén, K. Saeidi, Z. Shen, Hierarchical structures of stainless steel 316L manufactured by Electron Beam Melting, Addit. Manuf. 17 (2017) 106–112, https://doi.org/10.1016/j.addma.2017.07.003.

[16] J. Yin, D. Wang, H. Wei, L. Yang, L. Ke, M. Hu, W. Xiong, G. Wang, H. Zhu, X. Zeng, Dual-beam laser-matter interaction at overlap region during multi-laser powder bed fusion manufacturing, Addit. Manuf. 46 (2021) 102178, https://doi.org/10.1016/j.addma.2021.102178.

[17] M. Song, M. Wang, X. Lou, R.B. Rebak, G.S. Was, Radiation damage and irradiation-assisted stress corrosion cracking of additively manufactured 316L stainless steels, J. Nucl. Mater. 513 (2019) 33–44, https://doi.org/10.1016/j.jnucmat.2018.10.044.

[18] G. Meric de Bellefon, K.M. Bertsch, M.R. Chancey, Y.Q. Wang, D.J. Thoma, Influence of solidification structures on radiation-induced swelling in an additively-manufactured austenitic stainless steel, J. Nucl. Mater. 523 (2019) 291–298, https://doi.org/10.1016/j.jnucmat.2019.06.012.

[19] L.T. Liu, Y.Z. Li, K.P. Yu, M.Y. Zhu, H. Jiang, P. Yu, M.X. Huang, A novel stainless steel with intensive silver nanoparticles showing superior antibacterial property, Mater. Res. Lett. 9 (2021) 270–277, https://doi.org/10.1080/21663831.2021.1894613.

[20] E. Liverani, S. Toschi, L. Ceschini, A. Fortunato, Effect of selective laser melting (SLM) process parameters on microstructure and mechanical properties of 316L austenitic stainless steel, J. Mater. Process. Technol. 249 (2017) 255–263, https://doi.org/10.1016/j.jmatprotec.2017.05.042.

[21] Q. Chao, V. Cruz, S. Thomas, N. Birbilis, P. Collins, A. Taylor, P.D. Hodgson, D. Fabijanic, On the enhanced corrosion resistance of a selective laser melted austenitic stainless steel, Scr. Mater. 141 (2017) 94–98, https://doi.org/10.1016/j.scriptamat.2017.07.037.

[22] I.A. Segura, L.E. Murr, C.A. Terrazas, D. Bermudez, J. Mireles, V.S.V. Injeti, K. Li, B. Yu, R.D.K. Misra, R.B. Wicker, Grain boundary and microstructure engineering of Inconel 690 cladding on stainless-steel 316L using electron-beam powder bed fusion additive manufacturing, J. Mater. Sci. Technol. 35 (2019) 351–367, https://doi.org/10.1016/j.jmst.2018.09.059.

[23] Z. Shang, C. Fan, J. Ding, S. Xue, A. Gabriel, L. Shao, T. Voisin, Y.M. Wang, T. Niu, J. Li, T.D. Rubia, H. Wang, X. Zhang, Heavy ion irradiation response of an additively manufactured 316LN stainless steel, J. Nucl. Mater. 546 (2021) 152745, https://doi.org/10.1016/j.jnucmat.2020.152745.

[24] Z. Shang, C. Fan, S. Xue, J. Ding, J. Li, T. Voisin, Y.M. Wang, H. Wang, X. Zhang, Response of solidification cellular structures in additively manufactured 316 stainless steel to heavy ion irradiation: an in situ study, Mater. Res. Lett. 7 (7) (2019) 290–297, https://doi.org/10.1080/21663831.2019.1604442.

[25] X. Sun, F. Chen, H. Huang, J. Lin, X. Tang, Effects of interfaces on the helium bubble formation and radiation hardening of an austenitic stainless steel achieved by additive manufacturing, Appl. Surf. Sci. 467–468 (2019) 1134–1139, https://doi.org/10.1016/j.apsusc.2018.10.268.

[26] J. Lin, F. Chen, X. Tang, J. Liu, S. Shen, G. Ge, Radiation-induced swelling and hardening of 316L stainless steel fabricated by selected laser melting, Vacuum 174 (2020) 109183, https://doi.org/10.1016/j.vacuum.2020.109183.

[27] S. Li, J. Hu, W. Chen, J. Yu, M. Li, Y. Wang, Evolution of cellular dislocation structures and defects in additively manufactured austenitic stainless steel under ion irradiation, Scr. Mater. 178 (2020) 245–250, https://doi.org/10.1016/j.scriptamat.2019.11.036.

[28] K.M. Bertsch, G. Meric de Bellefon, B. Kuehl, D.J. Thoma, Origin of dislocation structures in an additively manufactured austenitic stainless steel 316L, Acta Mater. 199 (2020) 19–33, https://doi.org/10.1016/j.actamat.2020.07.063.

[29] G.S. Was, Challenges to the use of ion irradiation for emulating reactor irradiation, J. Mater. Res. 30 (2015) 1158–1182, https://doi.org/10.1557/jmr.2015.73.

[30] R.E. Stoller, M.B. Toloczko, G.S. Was, A.G. Certain, S. Dwaraknath, F.A. Garner, On the use of SRIM for computing radiation damage exposure, Nucl. Instrum. Methods Phys. Res., Sect. B 310 (2013) 75–80, https://doi.org/10.1016/j.nimb.2013.05.008.

[31] S. Plimpton, Fast parallel algorithms for short-range molecular dynamics, J Comp. Phys. 117 (1995) 1–19, https://doi.org/10.1006/jcph.1995.1039.

[32] G. Bonny, N. Castin, D. Terentyev, Interatomic potential for studying ageing under irradiation in stainless steels: the FeNiCr model alloy, Modell. Simul. Mater. Sci. Eng. 21 (8) (2013) 085004.

[33] P. Hirel, Atomsk: a tool for manipulating and converting atomic data files, Comput. Phys. Commun. 197 (2015) 212–219, https://doi.org/10.1016/j.cpc.2015.07.012.

[34] D. Kong, X. Ni, C. Dong, L. Zhang, C. Man, J. Yao, K. Xiao, X. Li, Heat treatment effect on the microstructure and corrosion behavior of 316L stainless steel fabricated by selective laser melting for proton exchange membrane fuel cells, Electrochim. Acta 276 (2018) 293–303, https://doi.org/10.1016/j.electacta.2018.04.188.

[35] X. Li, W. Liu, Y. Xu, C.S. Liu, Q.F. Fang, B.C. Pan, J.-L. Chen, G.-N. Luo, Z. Wang, An energetic and kinetic perspective of the grain-boundary role in healing radiation damage in tungsten, Nucl. Fusion 53 (12) (2013) 123014, https://doi.org/10.1088/0029-5515/53/12/123014.

[36] H. Huang, X. Tang, F. Chen, F. Gao, Q. Peng, L. Ji, X. Sun, Self-healing mechanism of irradiation defects in nickel–graphene nanocomposite: an energetic and kinetic perspective, J. Alloy. Compd. 765 (2018) 253–263, https://doi.org/10.1016/j.jallcom.2018.06.162.

[37] S.I. Wright, M.M. Nowell, D.P. Field, A review of strain analysis using electron backscatter diffraction, Microsc. Microanal. 17 (2011) 316–329, https://doi.org/10.1017/S1431927611000055.

[38] Y.M. Wang, T. Voisin, J.T. McKeown, J. Ye, N.P. Calta, Z. Li, Z. Zeng, Y. Zhang, W. Chen, T.T. Roehling, R.T. Ott, M.K. Santala, P.J. Depond, M.J. Matthews, A. V. Hamza, T. Zhu, Additively manufactured hierarchical stainless steels with high strength and ductility, Nat. Mater. 17 (2018) 63–71, https://doi.org/10.1038/nmat5021.

[39] K.G. Prashanth, J. Eckert, Formation of metastable cellular microstructures in selective laser melted alloys, J. Alloy. Compd. 707 (2017) 27–34, https://doi.org/10.1016/j.jallcom.2016.12.209.

[40] P.F. Zou, R.F.W. Bader, A topological definition of a Wigner-Seitz cell and the atomic scattering factor, Acta Cryst. 50 (1994) 714–725, https://doi.org/10.1107/S0108767394003740.

[41] A. Stukowski, Visualization and analysis of atomistic simulation data with OVITO – the open visualization tool, Modelling Simul. Mater. Sci. Eng. 18 (1) (2010) 015012.

[42] M. Godec, S. Zaefferer, B. Podgornik, M. Šinko, E. Tchernychova, Quantitative multiscale correlative microstructure analysis of additive manufacturing of stainless steel 316L processed by selective laser melting, Mater. Charact. 160 (2020) 1044–5803, https://doi.org/10.1016/j.matchar.2019.110074.

[43] A. Stukowski, K. Albe, Extracting dislocations and non-dislocation crystal defects from atomistic simulation data Modelling Simul, Mater. Sci. Eng. 18 (8) (2010) 085001.

[44] L. Cui, F. Jiang, D. Deng, T. Xin, X. Sun, R.T. Mousavian, R.L. Peng, Z. Yang, J. Moverare, Cyclic response of additive manufactured 316L stainless steel: The role of cell structures, Scr. Mater. 205 (2021) 1359–6462, https://doi.org/10.1016/j.scriptamat.2021.114190.

[45] A.M. Brockway, J. Schrier, Noble gas separation using PG-ESX (X = 1, 2, 3) nanoporous two-dimensional polymers, J. Phys. Chem. C 117 (2013) 393–402, https://doi.org/10.1021/jp3101865.

[46] Y.-J. Chen, B. Yu, Y. Zou, B.-N. Chen, W.-Q. Tao, Study on the effect of foreign particle on bubble nucleation by using molecular dynamics simulation, J. Mol. Liq. 305 (2020) 112876, https://doi.org/10.1016/j.molliq.2020.112876.

[47] G. Ackland, Controlling radiation damage, Science 327 (2010) 1587–1588, https://doi.org/10.1126/science.1188088.

[48] T. Voisin, J.-B. Forien, A. Perron, S. Aubry, N. Bertin, A. Samanta, A. Baker, Y. M. Wang, New insights on cellular structures strengthening mechanisms and thermal stability of an austenitic stainless steel fabricated by laser powder-bed-fusion, Acta Mater. 203 (2021) 1359–6454, https://doi.org/10.1016/j.actamat.2020.11.018.